Monthly Notices of the ROYAL ASTRONOMICAL SOCIETY

MNRAS **524,** 4447–4454 (2023)
Advance Access publication 2023 July 19

https://doi.org/10.1093/mnras/stad2170

Helium as a signature of the double detonation in Type Ia supernovae

Christine E. Collins [1,2]★ Stuart A. Sim,[2] Luke. J. Shingles [1,2] Sabrina Gronow,[3,4] Friedrich K. Röpke,[4,5] Rüdiger Pakmor [6] Ivo R. Seitenzahl [7] and Markus Kromer[4]

[1]*GSI Helmholtzzentrum für Schwerionenforschung, Planckstraße 1, D-64291 Darmstadt, Germany*
[2]*Astrophysics Research Center, School of Mathematics and Physics, Queen's University Belfast, Belfast BT7 1NN, UK*
[3]*Zentrum für Astronomie der Universität Heidelberg, Astronomisches Rechen-Institut, Mönchhofstr. 12-14, D-69120 Heidelberg, Germany*
[4]*Heidelberger Institut für Theoretische Studien, Schloss-Wolfsbrunnenweg 35, D-69118 Heidelberg, Germany*
[5]*Zentrum für Astronomie der Universität Heidelberg, Institut für theoretische Astrophysik, Philosophenweg 12, D-69120 Heidelberg, Germany*
[6]*Max-Planck-Institut für Astrophysik, Karl-Schwarzschild-Str. 1, D-85748 Garching, Germany*
[7]*School of Science, University of New South Wales, Australian Defence Force Academy, Canberra, ACT 2600, Australia*

Accepted 2023 July 17. Received 2023 July 17; in original form 2023 May 9

ABSTRACT

The double detonation is a widely discussed mechanism to explain Type Ia supernovae from explosions of sub-Chandrasekhar mass white dwarfs. In this scenario, a helium detonation is ignited in a surface helium shell on a carbon/oxygen white dwarf, which leads to a secondary carbon detonation. Explosion simulations predict high abundances of unburnt helium in the ejecta, however, radiative transfer simulations have not been able to fully address whether helium spectral features would form. This is because helium can not be sufficiently excited to form spectral features by thermal processes, but can be excited by collisions with non-thermal electrons, which most studies have neglected. We carry out a full non-local thermodynamic equilibrium radiative transfer simulation for an instance of a double detonation explosion model, and include a non-thermal treatment of fast electrons. We find a clear He I λ10830 feature which is strongest in the first few days after explosion and becomes weaker with time. Initially this feature is blended with the Mg II λ10927 feature but over time separates to form a secondary feature to the blue wing of the Mg II λ10927 feature. We compare our simulation to observations of iPTF13ebh, which showed a similar feature to the blue wing of the Mg II λ10927 feature, previously identified as C I. Our simulation shows a good match to the evolution of this feature and we identify it as high velocity He I λ10830. This suggests that He I λ10830 could be a signature of the double detonation scenario.

Key words: radiative transfer – line: formation – methods: numerical – white dwarfs – transients: supernovae.

1 INTRODUCTION

Type Ia supernovae (SNe Ia) are the thermonuclear explosion of a white dwarf, but the exact mechanism by which the white dwarf explodes is not yet fully understood. The double detonation is a promising scenario to explain SNe Ia for a range of luminosities. In this scenario, a helium detonation is ignited in a helium shell on a carbon–oxygen white dwarf. The helium detonation then ignites a secondary carbon detonation in the core. Early double detonation models (see e.g. Nomoto 1980, 1982; Taam 1980; Livne 1990; Woosley & Weaver 1994; Höflich & Khokhlov 1996; Nugent et al. 1997) invoked relatively massive helium shells (∼0.2 $M_\odot$), and predicted light curves and spectra that were not consistent with those of normal SNe Ia, due to over production of iron group elements in the outer ejecta. There has been renewed interest in the double detonation following suggestions that considerably lower mass helium shells (<0.1 $M_\odot$) may be able to ignite a secondary core detonation (Bildsten et al. 2007; Shen & Bildsten 2009; Fink et al. 2010; Shen et al. 2010), and significantly reduce the discrepancies with observations caused by the over-production of iron group elements at high velocities, produced in the helium shell detonation (Kromer et al. 2010; Woosley & Kasen 2011). Simulations by Townsley et al. (2019) and Shen et al. (2021) have suggested that by considering minimal helium shell masses, double detonations may be able to account for normal SNe Ia, although Collins et al. (2022) show that a minimal He shell mass does not necessarily lead to good agreement with normal SNe Ia. Additionally, Glasner et al. (2018) have shown for the first time conditions leading to the ignition of a helium detonation in an accreted helium envelope on top of a carbon–oxygen white dwarf.

A number of objects have recently been observed that have specifically been suggested to be produced by helium shell detonations, for example SN 2016jhr (Jiang et al. 2017) and SN 2018byg (De et al. 2019). These objects showed early peaks in their light curves, suggested to be the result of radioactive material produced in the outer layers of the ejecta. This has been predicted as a signature of a double detonation by Noebauer et al. (2017). Here, however, we consider a different potential signature of a double detonation. We investigate whether He spectral features could be directly detected. Double detonation simulations predict fairly large amounts of unburnt helium at high velocities in the outer layers of the SN ejecta (Fink et al. 2010; Shen & Moore 2014; Gronow et al. 2020, 2021). In each of the double detonation models presented by Fink et al. (2010), approximately

★ E-mail: c.collins@gsi.de

half of the initial helium shell mass was ejected as unburnt helium. Radiative transfer simulations have not been able to predict whether helium features should be able to form for the recent generation of double detonation simulations considering low-mass helium shells (e.g. Kromer et al. 2010; Woosley & Kasen 2011; Polin, Nugent & Kasen 2019; Townsley et al. 2019; Gronow et al. 2020; Shen et al. 2021; Collins et al. 2022; Pakmor et al. 2022), as these studies did not carry out full non-local thermodynamic equilibrium (non-LTE) simulations including non-thermal processes.

The ionization and excitation rates of helium are strongly affected by collisions with non-thermal electrons, and therefore to make predictions of helium spectral features, non-LTE radiative transfer simulations are required, and must account for non-thermal processes. Non-thermal electrons are produced by gamma-rays from the decays of ^{56}Ni. The importance of collisions with non-thermal electrons on the formation of helium features has been demonstrated for Type Ib/Ic supernovae (Chugai 1987; Lucy 1991; Hachinger et al. 2012).

Non-LTE simulations by Dessart & Hillier (2015) for a helium shell detonation model by Waldman et al. (2011) clearly showed that He spectral features form, where radiative transfer calculations are non-LTE and include non-thermal effects. This model, however, did not consider a secondary core detonation, and therefore the composition of the ejecta is different to the composition predicted for the double detonation scenario. In particular, this model predicted large amounts of helium at all velocities, whereas the double detonation predicts helium predominantly at high velocities (see e.g. Fink et al. 2010). The predicted spectral properties of the helium detonation model were classified as a hybrid Type Ia/Ib due to the clear detection of helium features.

Boyle et al. (2017) investigated whether helium spectral features could form for the recent generation of double detonation models with relatively low-mass helium shells (e.g. the models of Fink et al. 2010). In this study, Boyle et al. (2017) used an analytic approximation to estimate the excited He I level populations, and found that the He I 10 830 Å and 2 μm lines may be produced by high velocity He ($\sim$19 000 km s^{-1}). They note that since the He I 10 830 Å is substantially blueshifted, it may be blended with the blue wing of the Mg II 10 927 Å feature. Further, more detailed simulations are required to confirm this result, but this suggests that He I spectral features may be observable for this scenario, and indeed recently Dong et al. (2022) showed that SN 2016dsg had an absorption line around 9700–10 500 Å which they find is consistent with the He I 10 830 Å feature predicted by Boyle et al. (2017).

Liu et al. (2023) have pointed out that SN 2022jgb and other candidate thick helium-shell detonation SN 2018byg-like SNe (De et al. 2019) show a prominent absorption feature at $\sim$1μm, which Liu et al. (2023) suggest could be high-velocity ($\sim$26 000 km s^{-1}) He λ10830. Previous works have also attempted to identify helium spectral features in the near-IR spectra of SNe Ia (Höflich & Khokhlov 1996; Meikle et al. 1996; Mazzali & Lucy 1998; Marion et al. 2003, 2009). Marion et al. (2009) present a large sample of near-IR spectra of normal SNe Ia and do not find any clear detections of the strongest lines expected for He I, at 10 830 Å and 2 μm. However, they also do not detect C I in any of the spectra, which has since possibly been identified in near-IR spectra (Hsiao et al. 2013; Marion et al. 2015; Hsiao et al. 2015b; Wyatt et al. 2021). Wyatt et al. (2021) consider whether their C I detections could be misidentified He I. Following discussion of simulations by Boyle et al. (2017), Wyatt et al. (2021) conclude that it is unlikely the feature is He I, given that in the simulations of Boyle et al. (2017), helium absorption is visible at maximum light and grows stronger with time, whereas the observed feature becomes weaker toward maximum light. Additionally, the observed spectra show optical C II 6580 Å, confirming the presence of carbon in the SN ejecta. While the lower mass model considered by Boyle et al. (2017) does clearly show a trend of increasing He I 10 830 Å strength, the higher mass model predicts that the He I 10 830 Å feature remains a similar strength to the Mg II 10 927 Å feature. This indicates that the evolution of potential He features is likely model dependent, and requires further study. The approximate non-LTE treatment used by Boyle et al. (2017) assumes that the He II population is dominant. One limiting factor for this approximation is whether the non-thermal ionization rate remains sufficiently high that the helium remains ionized. Therefore, the strengths of the predicted features provide upper limits on the potential strength of helium features. In this work, the ionization state is calculated self-consistently, and can therefore better constrain the predicted strength of potential helium features.

In this paper, we investigate the potential for He spectral features to form in the double detonation explosion scenario, and whether these features could be detected in observations. The presence of He in the ejecta is a fundamental prediction of the double detonation scenario, but it has not yet been fully addressed whether the He would produce an observable spectral feature for contemporary double detonation explosion simulations. If an observable He spectral feature is produced, then this could be direct observational evidence for the double detonation explosion scenario, allowing us to identify the class of explosion as well as the progenitor system. We consider an ejecta profile from a hydrodynamical simulation of the double detonation, which we describe in Section 2.2. In Section 3.1, we present the simulated spectra, focusing specifically on predictions of He spectral features. We discuss how this simulation compares to observations of a SN Ia that showed similar behaviour to our simulation in Section 3.2.2, suggesting that He may have already been detected in SNe Ia, but misidentified.

2 METHODS

2.1 Non-LTE and non-thermal radiative transfer

We use the time-dependent multi-dimensional Monte Carlo radiative transfer code ARTIS (Sim 2007; Kromer & Sim 2009; Bulla, Sim & Kromer 2015, based on the methods of Lucy 2002, 2003, 2005). ARTIS has been extended by Shingles et al. (2020) to solve the non-LTE population and ionization balance, including ionizing collisions with fast non-thermal electrons. ARTIS solves the Spencer–Fano equation (as framed by Kozma & Fransson 1992) to trace the energy distribution of high-energy leptons seeded by high-energy particles emitted in radioactive decays. Similarly to Shingles et al. (2020), we allow Auger electrons to contribute to heating, ionization, and excitation. We do not include excitation of bound electrons by non-thermal collisions, since this is particularly computationally demanding, however, Hachinger et al. (2012) show that their results for He are rather insensitive to the excitation rates.

For photoionization, ARTIS uses the full Monte Carlo photon-packet trajectories (following Lucy 2003) to obtain a rate estimator for each level pair. For all other atomic processes, a parametrized radiation field is used to estimate transition rates. We use an atomic data set based on the compilation of CMFGEN (Hillier 1990; Hillier & Miller 1998, see Shingles et al. 2020 for details).

The radiative transfer simulations are carried out between 2 and 32 d after explosion, using 111 logarithmically spaced time steps. The initial time steps are in LTE and at time step 12 (2.7 d) the non-LTE solver is switched on.

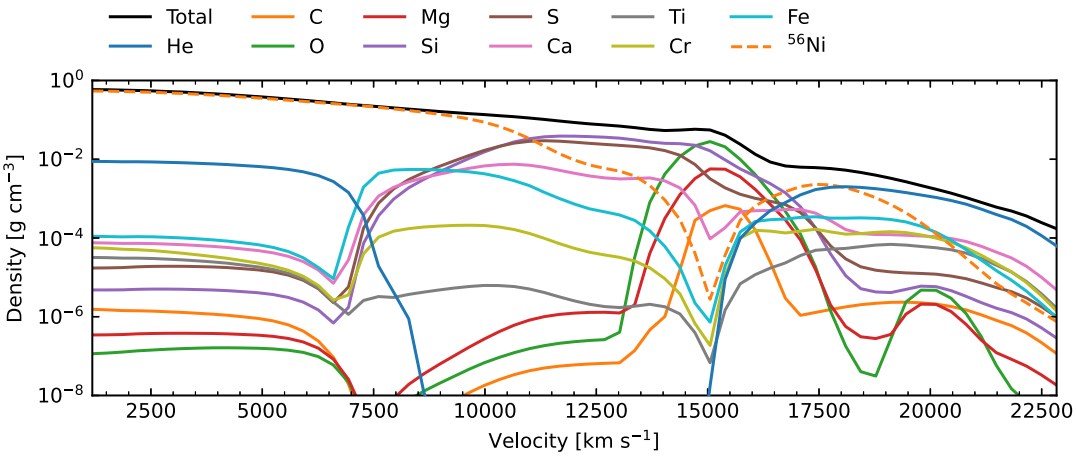

Figure 1. Model densities at 100 s after explosion.

2.2 Double detonation ejecta model

The ejecta model we consider in this work is based on the 3D double detonation explosion model M2a, described by Gronow et al. (2020). The light curves predicted for this model were of normal SNe Ia brightness, similar to SN 2011fe (Nugent et al. 2011). We therefore select this model to investigate the potential for He spectral features to form in normal brightness SNe Ia. We construct a 1D model from a slice of model M2a in an equatorial line of sight. Although ARTIS can perform multi-dimensional simulations, the performance cost is substantial and requires sacrifices to the number of detailed photoionization estimators. We find that at early times, while the ejecta are optically thick, this 1D model produces light curves and spectra similar to those expected from a 3D simulation in this line of sight. However, after maximum light, as the ejecta become more optically thin, we find that this model is no longer such a good representation of the 3D line of sight. Therefore, in this work we limit our calculations to the first few weeks after explosion. Since the He is predominantly found in the outer ejecta, we expect that He features are more likely to form at early times. We show the composition of this model in Fig. 1. We note that low density, outer ejecta ($v > 23\,200$ km s^{-1}) are ignored since these quickly become optically thin and are not expected to affect the spectrum at the times we consider here. This allows for better spatial resolution of the ejecta at velocities important in forming the spectra. The ejecta in the equatorial line of sight of Model M2a that we have based our ejecta on extend to ∼25 000 km s^{-1}, however, in the polar lines of sight the ejecta extend to higher velocities of >30 000 km s^{-1} (see Gronow et al. 2020).

The initial white dwarf mass of Model M2a was 1.05 M$_\odot$, with a He shell of 0.073 M$_\odot$ (see Gronow et al. 2020 for model details). After explosion, the total mass of He in the ejecta of Model M2a was 0.028 M$_\odot$, and the mass of ^{56}Ni was 0.58 M$_\odot$. In the 1D model we consider here, the He mass is 0.018 M$_\odot$, and the ^{56}Ni mass is 0.49 M$_\odot$.

The radiative transfer simulations carried out by Gronow et al. (2020) did not include non-thermal ionization, and made approximate non-LTE calculations. Therefore, they could not address whether helium spectral features would be expected to form for these models. In this work we carry out a full non-LTE simulation and include non-thermal ionization (as implemented by Shingles et al. 2020), with the aim of investigating the effect of the more detailed treatment of ionization on the formation of He features for the double detonation scenario. In this work, we investigate only one model due to the high computational expense of these simulations.

The double detonation scenario leads to strong asymmetries, and therefore, in future, 3D simulations should be carried out to investigate observer angle dependencies. Additionally, the ejecta structure and synthesized abundances show strong variations with different masses of the initial He shell and C/O core (e.g. Fink et al. 2010; Boos et al. 2021; Gronow et al. 2021). It should also be investigated how the predicted He spectral features would vary in response to such differences in the ejecta structure.

3 RESULTS

3.1 Helium spectral features

In future work we will present the full results of this non-LTE simulation, but in this paper we limit discussion to the ability of this simulation to produce He spectral features. We note that a level of Monte Carlo noise is present in our model spectra.

We identify the presence of He features in our simulated spectra by tagging escaping Monte Carlo radiation packets with the ion with which they last interacted. By examining packets whose last interaction was with He, we can quantify the contribution of He to the synthetic spectra and identify the specific spectral features for which He is responsible.

3.1.1 NIR He I λ10830

We predominantly focus on the wavelength region around where the He I 10 830 Å (2^3S–2^3P) feature would form. We expect this to be the strongest He feature with the least blending from other spectral lines. In Fig. 2 we show the spectrum at these wavelengths at 5 d after explosion, and indicate the contributions of He I to the spectrum. In the radiative transfer simulation, we record details of the last interaction each Monte Carlo packet underwent before escaping the ejecta. For each wavelength bin in the synthetic spectrum the area under the spectrum is colour coded in proportion to the energy carried by packets in that wavelength bin whose last interaction was

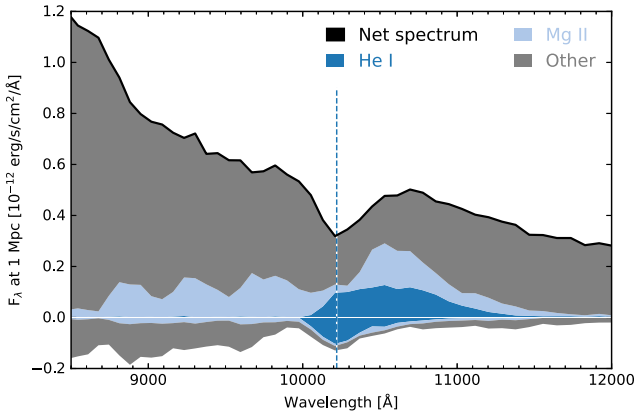

Figure 2. Spectrum at 5 d after explosion calculated using ARTIS including a non-thermal treatment. We show the contributions of He I and Mg II to the spectrum, and indicate the absorption by these ions beneath the axis. The wavelength of the minimum of the He I 10 830 Å feature is indicated by the dashed line. We note that no C I feature is formed.

with each of the ions considered. We also construct an equivalent histogram based on where the wavelength bin packets were prior to their last interaction (i.e. indicating where packets last underwent absorption/scattering/fluorescence) and plot this on the negative axis under the spectrum to indicate the key absorption processes. We find that the He I 10 830 Å feature is expected to form for this model, and that a relatively strong He absorption feature forms in the first few days after explosion. Over time the strength of this feature weakens, and at times later than ∼2 weeks after explosion this feature is no longer visible (see the spectral time series shown by Figs 3a–c).

In Fig. 2, showing the spectrum at 5 d after explosion, the He I 10 830 Å feature is initially completely blended with the Mg II 10 927 Å feature. In observations, this could be mistaken for a broad Mg II feature. In the region around the 10 830 Å feature, the emission from other lines is relatively weak, hence we find the 10 830 Å feature to be relatively strong. The 'Other' elements in Fig. 2 are predominantly intermediate mass elements, with the strongest contributions being from Si and S.

By 8 d after explosion, the He I feature has separated from the Mg II feature and is clearly distinguishable at the blue wing of the Mg II feature. The wavelength bin sizes have been chosen to minimize Monte Carlo noise in the model spectra. We note that the He I feature separating from the Mg II feature can be seen when using smaller wavelength bins. At 10 d after explosion, a distinct secondary feature to the blue wing of the Mg II feature can also be seen in Fig. 3(b), although this is weaker than at 8 d after explosion. At 5 d after explosion, the He I 10 830 Å feature is formed at ∼19 500 km s^{-1}, while the Mg II 10 927 Å feature is formed at ∼16 000 km s^{-1}. Over time, the velocity of the He I 10 830 Å feature decreases. At 2 weeks after explosion the feature is formed at ∼18 000 km s^{-1}.

Such features to the blue wing of the Mg II feature have previously been detected (Höflich et al. 2002; Hsiao et al. 2013, 2015b; Marion et al. 2015), but have been identified as C I 10 693 Å. This will be discussed further in Section 3.2.1. By two weeks after explosion, a clear He I 10 830 Å feature can no longer be seen, however, the blue wing of the Mg II feature is flattened due to He I 10 830 Å.

This demonstrates that near-infrared (NIR) He I 10 830 Å could be a signature of the double detonation explosion scenario, and that early NIR spectra are key to detecting the presence of this feature.

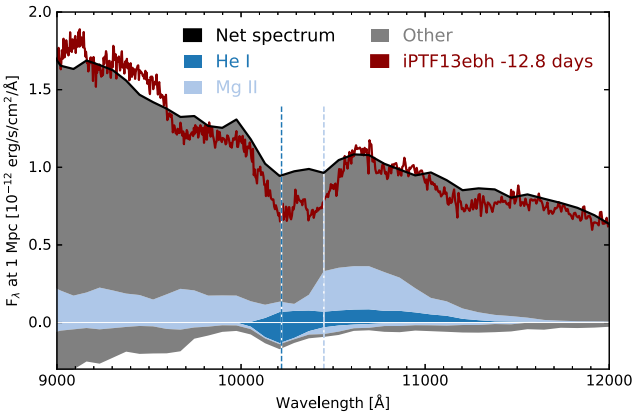

(a) 8 days after explosion.

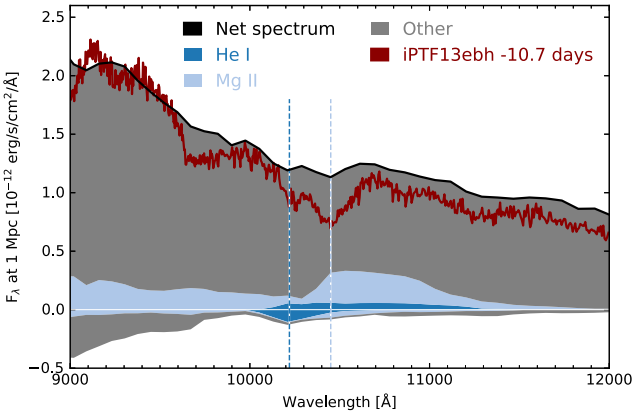

(b) 10 days after explosion.

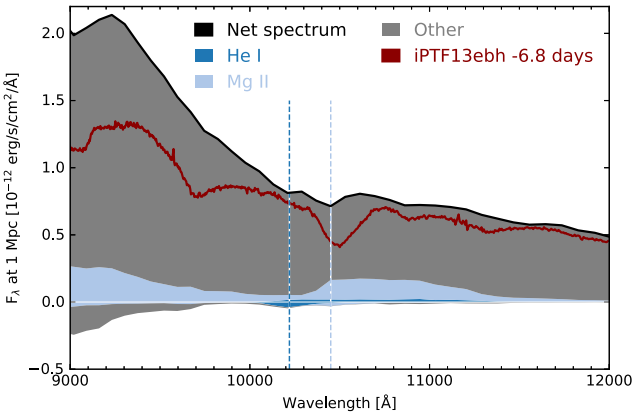

(c) 14 days after explosion.

Figure 3. Model spectra sequence showing the evolution of the He I 10 830 Å feature with time. The simulated time since explosion is noted below each model spectrum. The wavelengths of the minima of the He I 10 830 and Mg II 10 927 Å features are indicated by the dashed lines. We compare our model spectra to iPTF13ebh (Hsiao et al. 2015b). Since the time of explosion for this object is uncertain we list the observed times relative to *B*-band maximum of iPTF13ebh. The observed spectra have been scaled to be of similar brightness to our simulated spectra. We note that our model does not predict a C I feature.

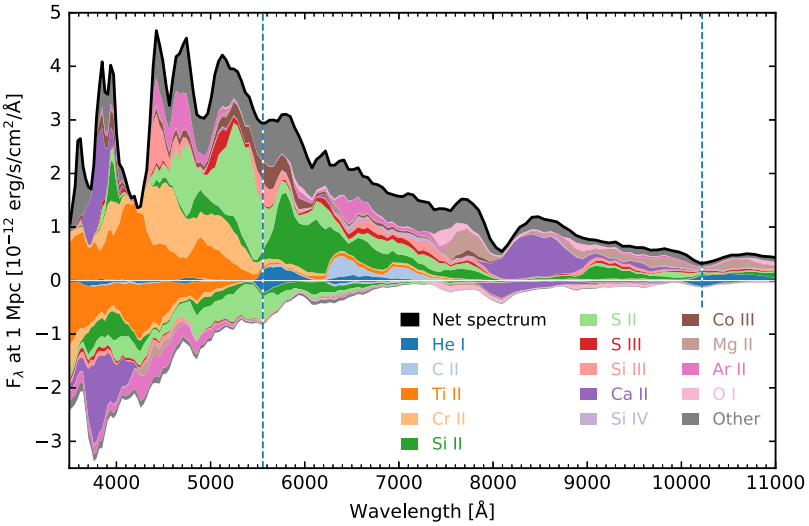

(a) 5 days after explosion. The dashed lines indicate the wavelengths of the He I absorption.

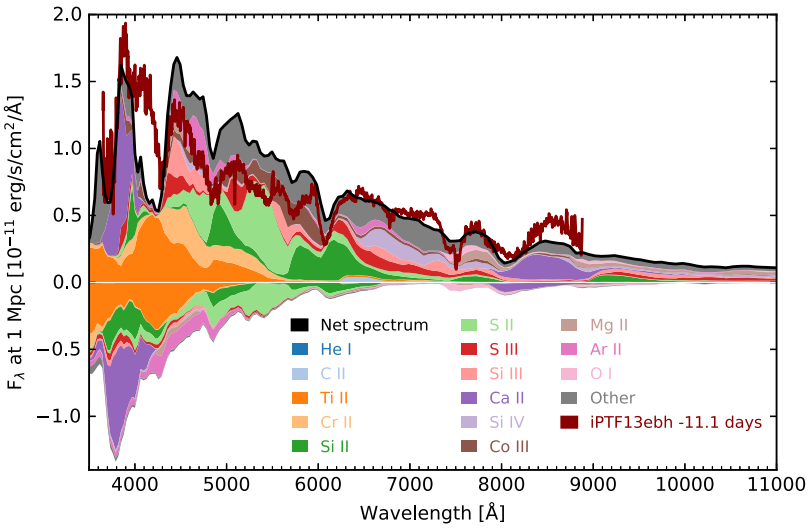

(b) 9 days after explosion.

Figure 4. Model optical spectra where the contributions of key species are indicated. We compare the spectrum at 9 d after explosion to the spectrum of iPTF13ebh (at 11.1 d before the observed *B*-band maximum light). The observed spectrum has been scaled to be of similar brightness to the simulated spectrum.

3.1.2 Optical He

We now discuss the presence of He features in the model optical spectra. At 5 d we find the He I 5876 Å feature to be the strongest optical He feature (see Fig. 4a), although, it is blended with other strong lines, predominantly from S II and Si II. A weak He I absorption feature is found at ∼5555 Å, however, this is blended with S II absorption. Similarly to the 10 830 Å feature, this is also strongest at the earliest times, and becomes weaker over time, however the 5876 Å feature fades more rapidly than the 10 830 Å, and is no longer formed by ∼9 d after explosion. Fig. 4(b) shows the key species contributing to the optical spectrum at 9 d after explosion, where contributions from He I can no longer be seen around 5876 Å. This shows that the He I 10 830 Å feature can be relatively strong without the expectation that the 5876 Å feature should also be strong. This was also noted by Mazzali & Lucy (1998), and Nugent et al. (1997) found no strong evidence for optical He lines in their calculations for a helium detonation model. We note that we find no He II features in our simulation.

3.1.3 He I 2 μm

Our model spectra show a high level of Monte Carlo noise in the wavelength region around 2 μm, where we would expect the He I 2 μm feature to form. Increasing the number of Monte Carlo packets in our simulation to improve the signal to noise at such red wavelengths is prohibitively computationally expensive at this time. We therefore cannot predict whether this model would produce a clear He I 2 μm feature. However, qualitatively, we find that there are contributions to the spectrum from He I in this wavelength region at very early times which decrease in strength with time and have faded by ∼1 week after explosion. We therefore suggest that it is possible that a He I 2 μm feature could form within the first week after explosion, however we cannot confirm this with our current simulation.

3.2 Discussion

We have shown for a particular instance of a double detonation model that the formation of a clear He I 10 830 Å feature is predicted

by our radiative transfer calculations. Future simulations should investigate whether this is a prediction of all double detonation models. Importantly, we do not expect a clear He feature in the optical spectra, implying that the non-detection of an optical He spectral feature can not be used to rule out the presence of He when identifying a He I 10 830 Å feature.

The He shell in this model before ignition was relatively massive (compared to that considered by Townsley et al. 2019, or the minimal He shell models presented by Gronow et al. 2021 and Boos et al. 2021), and so has more He in the ejecta at a more extended range of velocities than would be synthesized for a model with a thinner He shell. Additionally, the 3D model M2a (Gronow et al. 2020) on which our 1D model is based showed strong asymmetries. For example, He extends to higher velocities along the negative polar axis (see Gronow et al. 2020, fig. 13), in which case a He feature may form at higher velocities. Investigating the dependence of the strength and velocity of He features on the choice of model and observer orientation is beyond the scope of this work, however, it is likely that both the mass of He, and the mass of ^{56}Ni mixed with the He will influence the predicted He spectral features. In our model, ^{56}Ni is synthesized in the He shell detonation, and the presence of ^{56}Ni in the ejecta in the same regions as the He likely increases the number of non-thermal collisions with He. Future simulations should investigate the sensitivity of the line formation to the degree of mixing of ^{56}Ni with the He.

It is interesting that we find the He features become weaker with time, given that in simulations of SNe Ib this feature is found to grow in strength with time (Hachinger et al. 2012; Teffs et al. 2020), and also grows in strength in the He shell detonation model of Dessart & Hillier (2015). The He in the SNe Ib simulations, and in the He shell detonation model, extends over a wide range of velocities. In our simulation, however, the He is limited to a smaller range of velocities (see Fig. 1) in the outer ejecta. In the model considered by Dessart & Hillier (2015) He is the most abundant element at all velocities (see their Fig. 1) and they have more He by mass than in our model. Dessart & Hillier (2015) find that He I 10 830 Å is strong at all times beyond 5 d. They also find He I 5875 Å is clearly visible between 5 and 15 d until line blanketing by Ti II causes the feature to fade. It is possible that the He I 10 830 Å feature remained visible at all times due to the high abundance of He present at all velocities, and that the strengths of the He I features were found to be so strong due to the higher abundance of He in the model. Future work should investigate how model structure, and masses of He affect predictions of He spectral features.

Boyle et al. (2017) consider both a low-mass model (0.58 $M_\odot$ CO core and 0.21 $M_\odot$ He shell) and a high-mass model (1.025 $M_\odot$ CO core and 0.055 $M_\odot$ He shell). Like our model, the high-mass model shows a deficit of He at intermediate velocities, however, their low-mass model does not show this (see Fig. 3 of Boyle et al. 2017). Their low-mass model predicts that the He I 10 830 Å feature clearly grows in strength, and becomes much stronger than the Mg II 10 927 Å feature. In the high-mass model, however, the He I 10 830 Å feature becomes slightly stronger with time, but remains similar in strength to the Mg II 10 927 Å feature (fig. 11 of Boyle et al. 2017). The approximate non-LTE treatment used by Boyle et al. (2017) assumed that the He II population is dominant. In our simulation we find that indeed He II is the dominant ionization state in the outer ejecta throughout our simulation. Generally, He I is the next most highly populated in the outer ejecta.

3.2.1 NIR C I

A number of detections of a feature to the blue wing of the Mg II feature (similar to our simulated He I 10 830 Å feature) have been reported, which have previously been suggested to be C I. Specifically, clear features were identified in SN 1999by (Höflich et al. 2002), iPTF13ebh (Hsiao et al. 2015b), SN 2015bp (Wyatt et al. 2021), and SN 2012ij (Li et al. 2022), and an additional feature affecting the blue wing of the Mg II feature has been reported in SN 2011fe (Hsiao et al. 2013) and SN 2014J (Marion et al. 2015).

Hsiao et al. (2015b) claim the feature in the blue wing of the Mg II feature in iPTF13ebh is C I (see Section 3.2.2 below). Wyatt et al. (2021) and Liu et al. (2023) have detected similar features in SN 2015bp and SN 2012ij, respectively, for which they also propose identification with C I. These objects were classified as transitional SNe Ia, showing similar spectral properties to 91bg-like SNe, but also showing secondary NIR maxima, which also includes objects such as SN 1986G (Phillips et al. 1987), SN 2003gs (Krisciunas et al. 2009), and SN 2004eo (Pastorello et al. 2007; Mazzali et al. 2008). These have been suggested to link 91bg-like SNe to normal SNe Ia. Höflich et al. (2002) also identify the feature in SN 1999by as C I. SN 1999by is a 91bg-like, subluminous object, and the spectral evolution of this feature is similar to that in iPTF13ebh.

C I has tentatively been identified in the NIR spectra of the normal SN 2011fe (Hsiao et al. 2013), which showed a flattened wing to the Mg II feature. SN 2014J also showed a flattened wing similar to that in SN 2011fe, and was shown by Marion et al. (2015) to be a possible detection of C I. The feature in SN 2011fe showed an increase in strength towards maximum, however in iPTF13ebh it rapidly decreased in strength.

In our simulation we do not find any C I features. We do find contributions to the optical spectra from C II 6580 and 7235 Å, but these are weak and would not be easily detectable as they are heavily blended with stronger lines (see Fig. 4a). At the times when our He I feature forms, even in the outer layers of our simulation ejecta where temperatures are coolest and the ejecta are the least highly ionized, C II is the dominant ionization stage, with C III being the next most abundant, indicating that in this region C III is recombining to C II. C I is significantly depopulated relative to both C II and C III (on the order of 5 mag lower ionization fraction). As such, we would not expect C I features to form. This is consistent with e.g. Tanaka et al. (2008) and Heringer et al. (2019) who also found C II to be the dominant ionization state, rather than C I. However, note that some simulations have found that C I features can form (e.g. Höflich et al. 2002; Hsiao et al. 2015b).

3.2.2 Comparison of simulated spectra to observations

We compare our simulated spectra to those of iPTF13ebh (Hsiao et al. 2015b), which showed a clear second component to the blue wing of the Mg II feature in the early NIR spectra, and was identified as C I 10 693 Å. We chose this object given the high quality NIR spectra obtained at early times. It also showed similar peak brightnesses to our model (see Table 1). We note that we have not tuned our model in any way to try to match the spectra of iPTF13ebh. We are comparing our prediction based on an existing double detonation ejecta model to the observations of iPTF13ebh given the similarities between our simulated He I 10 830 Å feature and the observed feature (previously identified as C I) in iPTF13ebh.

iPTF13ebh has a Δm_{15}(B) value of 1.79 and is therefore in the fast-declining SN Ia category, but is classified as a transitional event: the photometric properties of iPTF13ebh place it in the category of

Table 1. Peak light-curve brightnesses for iPTF13ebh from Hsiao et al. (2015b), compared to the values calculated for our model.

	iPTF13ebh	Model
$M_{\rm u,max}$	-18.34 ± 0.19	-18.2
$M_{\rm B,max}$	-18.95 ± 0.19	-18.9
$M_{\rm V,max}$	-19.01 ± 0.18	-19.1
$M_{\rm g,max}$	-19.03 ± 0.18	-19.1
$M_{\rm r,max}$	-18.99 ± 0.18	-18.8
$M_{\rm i,max}$	-18.52 ± 0.18	-18.3
$M_{\rm J,max}$	-18.75 ± 0.18	-18.4
$M_{\rm H,max}$	-18.59 ± 0.18	-18.7

normal SNe Ia, however its spectral properties resemble those of SN 1999by which is a member of the 91bg-like class. iPTF13ebh however, showed no apparent Ti II features and is therefore not considered a 91bg-like object.

Hsiao et al. (2015b) found no optical C I features in iPTF13ebh. They did, however, find evidence for a weak optical C II 6580 Å feature at approximately the same epoch, which they also found to weaken rapidly. They propose identification of C I 9093 Å as weak notches in the two earliest spectra, and suggest that C I 9406 and 11 754 Å features could be present in the spectra, but blending makes these detections uncertain.

Since the observed feature at the blue wing of the Mg II 10 927 Å feature in iPTF13ebh shows similar behaviour to the simulated high velocity He I 10 830 Å feature in our model and the feature, we compare our model to the early NIR spectra of iPTF13ebh (Hsiao et al. 2015a). All spectra have been dereddened and redshift corrected.

We plot the spectra of iPTF13ebh in Figs 3(a)–(c), along with our model spectra. We use times relative to maximum light for the observed spectra since the inferred time since explosion is uncertain (see Hsiao et al. 2015b). In the spectra of iPTF13ebh, the feature can be seen decreasing in strength over time until in Fig. 3(c) at 6.8 d before maximum it is barely visible. Maximum light in *B* band occurs in our simulation at ∼18.6 d after explosion. The He I feature predicted in our simulation is able to reproduce the blue wing of the Mg II feature in all three spectra, although at ∼2.2 d earlier than the times of the observed spectra. The velocities of the He I and Mg II features appear to be well matched, as well as the trend in strength of the He I feature relative to the Mg II feature.

Given this match between the evolution of our He I 10 830 Å feature and the feature in iPTF13ebh, as well as the lack of C I in our model spectra, we identify this feature as He I λ10 830, and suggest that this could be a signature of the double detonation scenario.

We show a comparison between the optical spectrum of our model at 9 d after explosion to the observed spectrum of iPTF13ebh in Fig. 4(b). Our model shows a Ti II trough at ∼4000–4500 Å which is not observed in iPTF13ebh, but apart from this feature the spectra show reasonable agreement. At this time our model does not predict any optical He I features, which is consistent with the observations of iPTF13ebh. We note that the spectra of iPTF13ebh have strong telluric absorption in the region around where the He I 2 μm feature could form (Hsiao et al. 2015b), and therefore we cannot identify whether this feature is present in the observed spectra.

4 CONCLUSIONS

We have shown for an instance of a double detonation explosion model that He I 10 830 Å is a predicted spectral feature. By including a non-thermal solution in our calculations, He I features are able to form for the double detonation scenario, and could be a signature of this explosion mechanism.

In our simulation, we find a clear absorption feature due to high velocity He I 10 830 Å. We find the He I 10 830 Å feature is strongest in the first few days after explosion, and becomes weaker over time. After two weeks, this feature is no longer visible. The He I 10 830 Å feature is initially blended with Mg II, and therefore could potentially be concealed in observed spectra. We find that over time the He I feature separates from the Mg II, such that we see two distinct features. We note, however, it is likely that the strength and evolution of the He I λ10830 feature is model dependent, and future studies should be carried out investigating different mass models.

We find that the He I 5876 Å feature is able to form in our simulation at very early times, however, this is blended with other strong lines and quickly fades. Therefore, the non-detection of this feature in the optical spectra should not be used to rule out the presence of the He I 10 830 Å feature, particularly later than the first week after explosion.

Due to Monte Carlo noise in our simulation around 2 μm we cannot confirm whether a clear He I 2 μm feature would form for this model. However, we do find He I contributions to the model spectra in this wavelength range indicating that a He I 2 μm feature could potentially form that would be strongest at early times and decrease in strength until ∼1 week after explosion.

In addition to our result that He I 10 830 Å is a predicted spectral feature for the double detonation scenario, we compare the simulated evolution of this feature to observations of iPTF13ebh, which we suggest showed evidence of a He I 10 830 Å feature. A secondary component at the blue wing of the Mg II λ10 927 feature has previously been observed in transitional SNe Ia, such as iPTF13ebh (Hsiao et al. 2015b), which showed a similar evolution to that predicted by the He I 10 830 Å feature in our model. However, this has previously been identified as C I 10 693 Å. We have compared our model spectra to the observations of iPTF13ebh and found that He I 10 830 Å can reproduce this feature, and we suggest that this is evidence for He I in SNe Ia and for the double detonation explosion scenario. This shows that He I may not always be concealed in the spectra of SNe Ia. In order to potentially detect the He I 10 830 Å in observations, and to identify this feature, early NIR observations are required.

ACKNOWLEDGEMENTS

CEC is grateful for support from the Department for the Economy (DfE) and acknowledges support by the European Research Council (ERC) under the European Union's Horizon 2020 research and innovation program under grant agreement no. 759253. CEC and LJS acknowledge support by Deutsche Forschungsgemeinschaft (DFG, German Research Foundation)—Project-ID 279384907 – SFB 1245 and MA 4248/3-1. The work of SAS was supported by the Science and Technology Facilities Council [grant numbers ST/P000312/1, ST/T000198/1, and ST/X00094X/1]. LJS acknowledges support by the European Research Council (ERC) under the European Union's Horizon 2020 research and innovation program (ERC Advanced Grant KILONOVA No. 885281). The work of SG and FKR was supported by the Deutsche Forschungsgemeinschaft (DFG, German Research Foundation) under Project-ID 138713538, SFB 881 ('The Milky Way System', Subproject A10), by the ChETEC ⟨0:fund ing-source 3:href="http://dx.doi.org/10.13039/501100000921"⟩CO ST⟨/0:funding-source⟩Action (CA16117), by the National Science Foundation under Grant No. OISE-1927130 (IReNA), and by the

Klaus Tschira Foundation. The authors gratefully acknowledge the Gauss Centre for Supercomputing e.V. (www.gauss-centre.eu) for funding this project by providing computing time on the GCS Supercomputer JUWELS at Jülich Supercomputing Centre (JSC). This work was performed using the Cambridge Service for Data Driven Discovery (CSD3), part of which is operated by the University of Cambridge Research Computing on behalf of the STFC DiRAC HPC Facility (www.dirac.ac.uk). The DiRAC component of CSD3 was funded by BEIS capital funding via STFC capital grants ST/P002307/1 and ST/R002452/1 and STFC operations grant ST/R00689X/1. DiRAC is part of the National e-Infrastructure. CEC is grateful for computational support by the VIRGO cluster at GSI. NUMPY and SCIPY (Oliphant 2007), MATPLOTLIB (Hunter 2007), and ARTISTOOLS[1] (Shingles et al. 2023) were used for data processing and plotting.

DATA AVAILABILITY

The spectra presented here will be made available on the Heidelberg supernova model archive HESMA[2] (Kromer, Ohlmann & Röpke 2017).

REFERENCES

Bildsten L., Shen K. J., Weinberg N. N., Nelemans G., 2007, ApJ, 662, L95
Boos S. J., Townsley D. M., Shen K. J., Caldwell S., Miles B. J., 2021, ApJ, 919, 126
Boyle A., Sim S. A., Hachinger S., Kerzendorf W., 2017, A&A, 599, A46
Bulla M., Sim S. A., Kromer M., 2015, MNRAS, 450, 967
Chugai N. N., 1987, Sov. Astron. Lett., 13, 282
Collins C. E., Gronow S., Sim S. A., Röpke F. K., 2022, MNRAS, 517, 5289
De K. et al., 2019, ApJ, 873, L18
Dessart L., Hillier D. J., 2015, MNRAS, 447, 1370
Dong Y. et al., 2022, ApJ, 934, 102
Fink M., Röpke F. K., Hillebrandt W., Seitenzahl I. R., Sim S. A., Kromer M., 2010, A&A, 514, A53
Glasner S. A., Livne E., Steinberg E., Yalinewich A., Truran J. W., 2018, MNRAS, 476, 2238
Gronow S., Collins C. E., Sim S. A., Röpke F. K., 2021, A&A, 649, A155
Gronow S., Collins C., Ohlmann S. T., Pakmor R., Kromer M., Seitenzahl I. R., Sim S. A., Röpke F. K., 2020, A&A, 635, A169
Hachinger S., Mazzali P. A., Taubenberger S., Hillebrand t W., Nomoto K., Sauer D. N., 2012, MNRAS, 422, 70
Heringer E., van Kerkwijk M. H., Sim S. A., Kerzendorf W. E., Graham M. L., 2019, ApJ, 871, 250
Hillier D. J., 1990, A&A, 231, 111
Hillier D. J., Miller D. L., 1998, ApJ, 496, 407
Höflich P., Gerardy C. L., Fesen R. A., Sakai S., 2002, ApJ, 568, 791
Höflich P., Khokhlov A., 1996, ApJ, 457, 500
Hsiao E. Y. et al., 2013, ApJ, 766, 72
Hsiao E. Y. et al., 2015a, VizieR Online Data Catalog: Optical and NIR spectra of SN iPTF13ebh,
Hsiao E. Y. et al., 2015b, A&A, 578, A9
Hunter J. D., 2007, Comput. Sci. Eng., 9, 90
Jiang J.-A. et al., 2017, Nature, 550, 80
Kozma C., Fransson C., 1992, ApJ, 390, 602
Krisciunas K. et al., 2009, AJ, 138, 1584
Kromer M., Ohlmann S., Röpke F. K., 2017, Mem. Soc. Astron. Ital., 88, 312
Kromer M., Sim S. A., 2009, MNRAS, 398, 1809
Kromer M., Sim S. A., Fink M., Röpke F. K., Seitenzahl I. R., Hillebrandt W., 2010, ApJ, 719, 1067
Li Z. et al., 2022, ApJ, 927, 142
Liu C. et al., 2023, ApJ, 946, 83
Livne E., 1990, ApJ, 354, L53
Lucy L. B., 1991, ApJ, 383, 308
Lucy L. B., 2002, A&A, 384, 725
Lucy L. B., 2003, A&A, 403, 261
Lucy L. B., 2005, A&A, 429, 19
Marion G. H. et al., 2015, ApJ, 798, 39
Marion G. H., Höflich P., Gerardy C. L., Vacca W. D., Wheeler J. C., Robinson E. L., 2009, AJ, 138, 727
Marion G. H., Höflich P., Vacca W. D., Wheeler J. C., 2003, ApJ, 591, 316
Mazzali P. A., Lucy L. B., 1998, MNRAS, 295, 428
Mazzali P. A., Sauer D. N., Pastorello A., Benetti S., Hillebrandt W., 2008, MNRAS, 386, 1897
Meikle W. P. S. et al., 1996, MNRAS, 281, 263
Noebauer U. M., Kromer M., Taubenberger S., Baklanov P., Blinnikov S., Sorokina E., Hillebrand t W., 2017, MNRAS, 472, 2787
Nomoto K., 1980, Space Sci. Rev., 27, 563
Nomoto K., 1982, ApJ, 253, 798
Nugent P. E. et al., 2011, Nature, 480, 344
Nugent P., Baron E., Branch D., Fisher A., Hauschildt P. H., 1997, ApJ, 485, 812
Oliphant T. E., 2007, Comput. Sci. Eng., 9, 10
Pakmor R. et al., 2022, MNRAS, 517, 5260
Pastorello A. et al., 2007, MNRAS, 377, 1531
Phillips M. M. et al., 1987, PASP, 99, 592
Polin A., Nugent P., Kasen D., 2019, ApJ, 873, 84
Shen K. J., Bildsten L., 2009, ApJ, 699, 1365
Shen K. J., Boos S. J., Townsley D. M., Kasen D., 2021, ApJ, 922, 68
Shen K. J., Kasen D., Weinberg N. N., Bildsten L., Scannapieco E., 2010, ApJ, 715, 767
Shen K. J., Moore K., 2014, ApJ, 797, 46
Shingles L. J. et al., 2020, MNRAS, 492, 2029
Shingles L. J., Collins C. E., Holas A., Callan F., Sim S., 2023, Artistools. Available at: https://github.com/artis-mcrt/artistools
Sim S. A., 2007, MNRAS, 375, 154
Taam R. E., 1980, ApJ, 242, 749
Tanaka M. et al., 2008, ApJ, 677, 448
Teffs J., Ertl T., Mazzali P., Hachinger S., Janka H. T., 2020, MNRAS, 499, 730
Townsley D. M., Miles B. J., Shen K. J., Kasen D., 2019, ApJ, 878, L38
Waldman R., Sauer D., Livne E., Perets H., Glasner A., Mazzali P., Truran J. W., Gal-Yam A., 2011, ApJ, 738, 21
Woosley S. E., Kasen D., 2011, ApJ, 734, 38
Woosley S. E., Weaver T. A., 1994, ApJ, 423, 371
Wyatt S. D. et al., 2021, ApJ, 914, 57

[1] https://github.com/artis-mcrt/artistools/
[2] https://hesma.h-its.org

This paper has been typeset from a TEX/LATEX file prepared by the author.